An Innovative Approach to Early Warning of Flashover via Pollution-Induced Radio Frequency Activity on High-Voltage Ceramic Insulators

Camilo Alvear Jorquera, Jorge Alfredo Ardila-Rey,
Bruno Albuquerque de Castro, Roger Schurch,
Johny Montaña , Carlos Boya

***Abstract*—Pollution on the surface of an insulator, combined with conditions such as fog, dew, or moisture, directly influences partial discharge (PD) activity, a key indicator of an insulator's aging process. Using an artificial pollution chamber, three classes of insulators were subjected to saline dew across multiple test runs, during which radio frequency emissions were recorded by an antenna. The contamination process was monitored and characterized using three indicators derived from the cumulative energy per interval, the cumulative average time between signals, and the cumulative distributed energy. By employing segmented regression analysis on these variables, it was possible to detect and quantify changes in PD activity as measured in the ultrahigh-frequency (UHF) band by a nearby antenna. Compared with galvanic, leakage-current-based approaches and artificial intelligence (AI)-based models, the proposed scheme has lower computational cost and provides operator tunable alert states for training-free, noncontact, trend-based early warning. In every test run, the developed algorithm identified at least one trend change by 80% of the test duration. Analyzing each trend change with the three indicators enabled graded alert states, demonstrating flexibility for assessing flashover (FO) risk. In all experiments conducted on the different types of insulators, FO consistently occurred during the highest alarm state.**

***Index Terms*—Antenna, flashover (FO), insulators, partial discharge (PD), ultrahigh-frequency (UHF) measurement.**

Received 24 November 2025; accepted 6 January 2026. Date of publication 30 January 2026; date of current version 20 February 2026. This work was supported in part by the National Agency for Research and Development (ANID) through the Project Fondef under Grant TA24I10002 and in part by the ANID Project Innovation Center for Sustainable Energy Transition (SET) under Grant CTI250019. The Associate Editor coordinating the review process was Dr. Logan M. Wilcox. *(Corresponding author: Jorge Alfredo Ardila-Rey.)*

Camilo Alvear Jorquera and Jorge Alfredo Ardila-Rey are with the Department of Electrical Engineering, Universidad Técnica Federico Santa María, Santiago 8940000, Chile (e-mail: camilo.alvearjorquera@postgrad.manchester.ac.uk; jorge.ardila@usm.cl).

Bruno Albuquerque de Castro is with the Department of Electrical Engineering, Sao Paulo State University, São Paulo 17033-360, Brazil (e-mail: bruno.castro@unesp.br).

Roger Schurch and Johny Montaña are with the Department of Electrical Engineering, Universidad Técnica Federico Santa María, Valparaíso 2340000, Chile (e-mail: roger.schurch@usm.cl; johny.montana@usm.cl).

Carlos Boya is with the Centro de Investigación e Innovación Educativa, Ciencia y Tecnología (CIIECYT-AIP), Tocumen, Panama City 07215, Panama, and also with the Instituto Tecnico Superior Especializado (ITSE), Tocumen, Panama City 07215, Panama (e-mail: carlos.boya@uip.pa).

Luis Orellana is with the Karlsruhe Institute of Technology (KIT), Institute for Pulsed Power and Microwave Technology (IHM), 76344 Eggenstein-Leopoldshafen, Germany (e-mail: luis.orellana@kit.edu).

I. Introduction

HIGH-VOLTAGE insulators play a fundamental role in electrical power transmission and distribution systems, as they provide electrical insulation between high-voltage components and the surrounding infrastructure. These devices form a barrier between the energized parts of an electrical circuit, preventing current flow to undesired conductive paths, even under extreme operating conditions [1]. Initially, ceramic and glass were the predominant materials used for electrical insulators, selected for their superior dielectric strength and resilience under adverse environmental conditions. However, with advancements achieved in recent decades in the field of new materials, the adoption of nonceramic composite insulators, especially those made of silicone rubber, has been broadened, offering improved performance and durability [2], [3].

One of the main stress factors that insulators are exposed to is environmental pollution, particularly in outdoor settings, which, in the presence of moisture, can lead to field concentration points, PD, and, in severe cases, FO events [4]. FO events on insulators have been extensively studied for over half a century, beginning with a model introduced by Obenaus [5]. This model provided a mathematical representation of the voltage applied to the insulator and the level of contamination to determine the thresholds at which an FO might occur [5], [6]. Over the years, this fundamental model has evolved to integrate advancements in the area of new materials, along with decades of accumulated experience, significantly influencing the design of many insulators currently being installed in the electrical network. Consequently, the main focus of numerous recent studies has increasingly shifted toward leveraging advanced diagnostic techniques, including real-time data analytics and machine learning, to assess the status of insulators under diverse environmental or operational conditions [7], [8], [9], [10].

As specified in IEC 60507, one of the artificial pollution test methods used on these devices is the fog method, in which the insulator is subjected to a defined environmental pollution. Another employed technique is the solid layer method, which involves depositing a uniform layer of defined solid pollution on the insulator's surface [11]. These two procedures have been widely used for studying and evaluating the insulator's performance in polluted environments. However, the literature also describes other contamination methods, thus broadening the scope of potential experimental conditions [12]. Based on the aforementioned, to quantify the pollution accumulated on the insulator, many studies have utilized the measurement of PD or the leakage current derived from the insulator's surface [13], [14], [15]. Other research has focused on less conventional methods, such as measuring the electromagnetic (EM) or acoustic emissions associated with the PD activity generated by the pollution and applied voltage [16], [17], [18].

Given the stochastic and nonlinear nature of these and other macroscopic effects generated throughout the insulator contamination process, the use of a diverse array of artificial intelligence (AI) algorithms is considered a suitable approach for managing the data obtained from any of the measurement techniques being used. This includes neural networks, support vector machines, decision trees, ensemble methods such as random forests and gradient boosting, as well as clustering algorithms used in unsupervised learning contexts [19]. The scientific literature details various studies that have employed these diverse AI methods to explore, in both general and specific terms, the levels of contamination or the probability of FO, reflecting ongoing efforts to establish their effectiveness in this domain [7], [8], [20], [21], [22]. However, much of this work relies primarily on the capability of the AI model rather than on generalizable, task-relevant parameters explicitly linked to the progression of contamination.

A common feature of AI algorithms, including both machine learning and deep learning, is the necessity of a prior training process [19]. While the choice of model architecture and techniques to ensure generalization are crucial, the performance of an AI model also depends on the quality, quantity, and relevance of the data used during training. This underscores the need to investigate methods that rely on generalizable indicators (requiring minimal site-specific tuning) and that, ideally, do not require additional training data or galvanic interaction with the asset under test.

Based on the foregoing, this article introduces an innovative methodology that utilizes three different indicators to preemptively flag potential FO events on insulators, as a response to the evolution of contamination on their surfaces. The novelty lies in combining three cumulative UHF-derived indicators with segmented-regression breakpoints (ψ) to detect trend changes and map them to operator-tunable alert states, enabling training-free, noncontact early warning with lower computational cost than AI-intensive approaches. Real-time data captured by an antenna monitoring UHF PD activity serve as the foundation for deriving these indicators, which exhibit a consistent behavior pattern across diverse measurement processes. As detailed in Section II, these indicators are derived from PD activity: the cumulative energy per intervals, the cumulative average time between signals, and the relationship between the cumulative energy per interval and the average time between signals nonaccumulated. Section III presents the results obtained with different classes of ceramic insulators subjected to various contamination processes, aiming to validate the performance of these indicators and their potential application in early fault warning systems. Finally, to emulate the operation of an early alert system, four alert states based on the three obtained indicators were established: *Normal*, *Attention*, *Warning*, and *Alarm*. Each state was used to classify the FO risk due to contamination under different scenarios. Throughout all measurement processes, it was observed that each FO event occurred within one of the established alert states, thus demonstrating the significant potential of these indicators to improve the ability to anticipate and respond to FO events.

II. Test Method

A. Experimental Setup

In each of the conducted experiments, the test conditions described in [7] were replicated. Specifically, at the beginning, four layers of contamination were deposited on the surface of the insulator. Each layer contained a mixture of 167 g of NaCl per liter of tap water. Before applying the subsequent layer, it was ensured that the preceding one was completely dry. Once this preconditioning phase was completed, the insulator was subjected to its nominal voltage according to its class and was periodically sprayed every 4 minutes with the same saline solution using a manual sprayer. Simultaneously, a 100 W halogen lamp remained lit above the test chamber to simulate the effect of drying on a sunny day, as depicted in Fig. 1. For each insulator, the test ended 1 or 2 minutes after the FO event, once a critical layer of contamination covered the surface of the insulator. This either caused the arc to self-extinguish or led the current to reach dangerous levels for the high-voltage transformer. At this point, the emergency stop button was pressed.

The EM emissions are recorded using a commercial directional open slot antenna, Deepace KC R102, with dimensions of 12 cm in height, 16.9 cm in length, and 1 mm in thickness, as shown in Fig. 2(a). According to the measured $S11$ parameter for this antenna [Fig. 2(b)], it is capable of capturing signals across the entire ultrahigh frequency (UHF) spectrum, but exhibits higher efficiency within the frequency range of 1500 to 2500 MHz. During each test, the antenna was positioned 50 cm from the object under test (OUT) and connected to the acquisition system (a Keysight Infiniium DSOS804A oscilloscope). The oscilloscope is configured to measure each PD pulse within a time window of 1 μs, with a sampling frequency of 5 GS/s, resulting in 5000 samples per signal. For each test, the same vertical scale is established, and the trigger level is set above the background EM noise present in the laboratory. In parallel, during each test, simultaneous PD monitoring was carried out with a commercial PD acquisition unit (TECHimp PDCheck) and a high-frequency current transformer (HFCT) to corroborate in real-time the presence of PDs on the insulator.

To supply high voltage in each of the measurement processes, an indirect circuit in accordance with IEC 60270 standard was used [23]. This circuit includes a high-voltage transformer of 400 V/150 kV connected to the industrial power grid of 220 V and 50 Hz, as illustrated in Fig. 1. Additionally, the insulator was connected in parallel to a low-impedance capacitive branch for high-frequency pulses

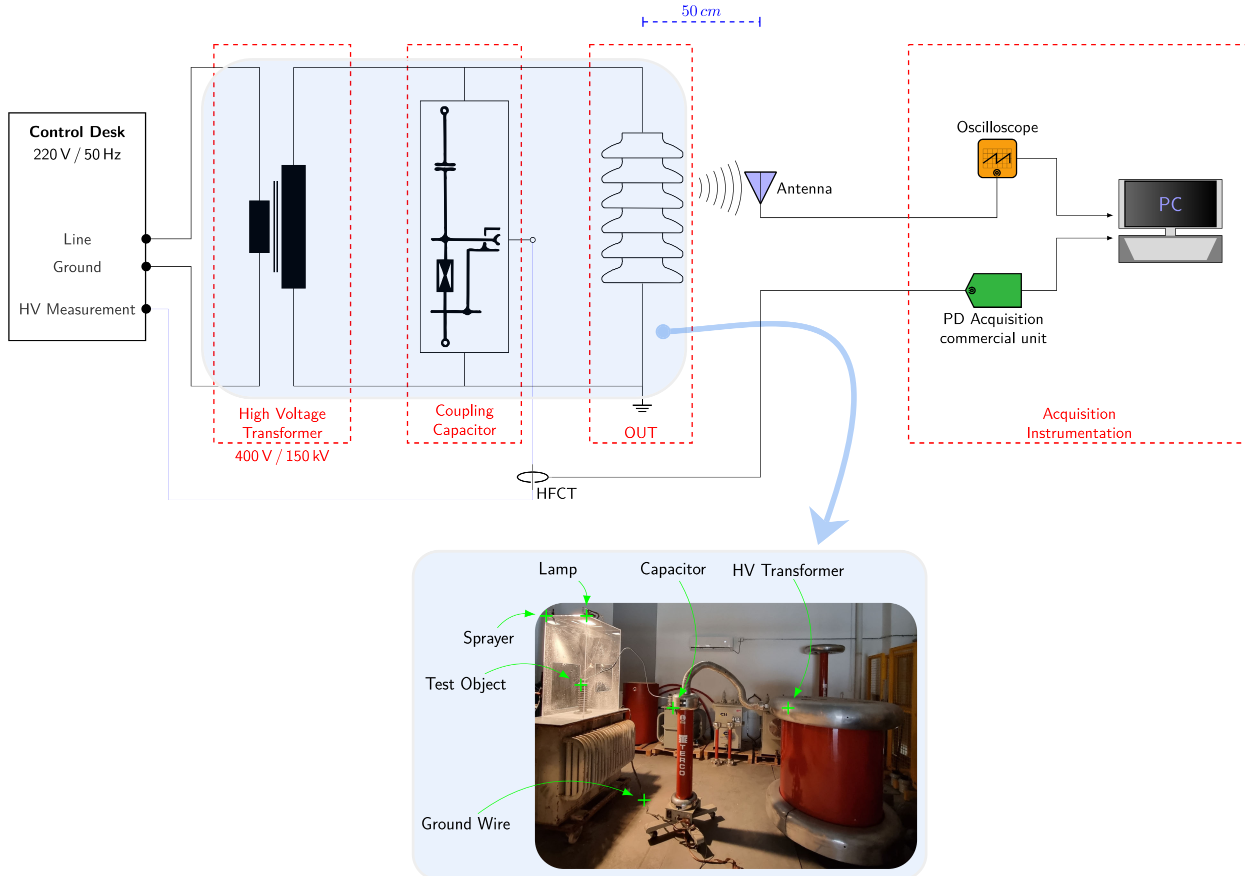

Fig. 1. Circuit diagram and laboratory setup used in the measuring procedure.

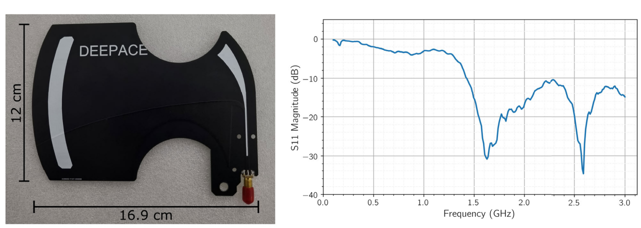

(a) (b)

Fig. 2. (a) Antenna dimensions and (b) S_{11} response.

(PD pulses), consisting of a 1 nF capacitor and a measuring impedance. This configuration allows a commercial PD detection system to continuously measure PD activity, thereby enabling monitoring throughout the measurement process for the presence or absence of PD sources.

B. Data Acquisition and Preprocessing

To record each of the signals, a Python script was developed that interacts with the segmented memory function of the oscilloscope. This setup allows for the storage of timestamps and amplitudes of the PD signals captured. Given the stochastic nature of the PD phenomena, the duration of a test may vary, ranging from less than an hour to a few hours. Therefore, for comparison purposes, the duration of each test is presented as a percentage of its total elapsed time to uniformly contrast every test trend across a common time domain, where the 100% mark corresponds to the end of the test. This representation does not imply that an analysis needs to specify the exact moment when the FO occurs or when the test concludes (as it does not make much sense in a real application).

For clarity, the 0%–100% normalization is used solely for cross-test visualization. In online operation, the time index corresponds to the available historical window at each update, and trend-change breakpoints are estimated on that window without any prior knowledge of the FO instant. As detailed in Section II-C, the final 5% represents the most recent data stream, whereas the preceding 95% is the historical record used for change detection. To illustrate this in a practical measurement context, we refer to one of the 13 measurement processes detailed in Table I (measurement process 4 marked with an asterisk). Fig. 3 depicts the number of signals captured over time, in minutes and as a percentage, including the moment when the FO occurs, represented by a translucent red area, and the 100% mark, depicted as a dot-dashed red line. The dots in this figure represent a measured signal, and the space between them, labeled as D_j, corresponds to the duration, in seconds, during which no signal was detected by the oscilloscope.

From numerous experimental measurements conducted in laboratory conditions with three types of insulators, which were contaminated over time, it was observed that, regardless

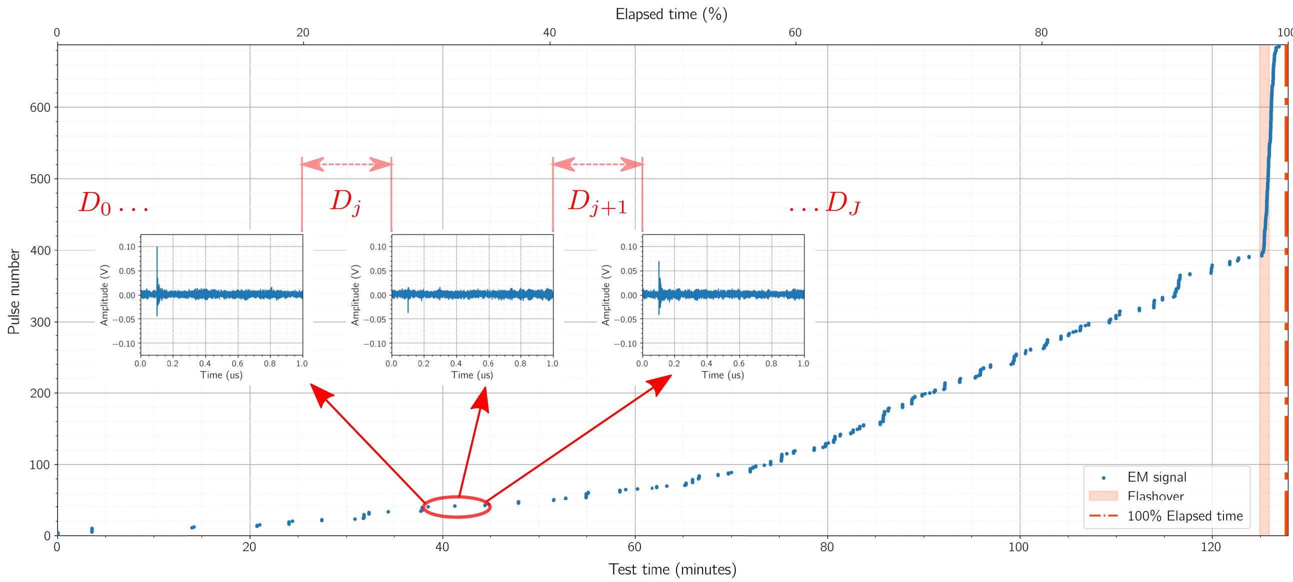

Fig. 3. Summary of the data acquisition model for a single test (example test 4*).

TABLE I
DETAILS OF TESTS FOR EACH INSULATOR CLASS (* TEST USED AS EXAMPLE)

Ins. Class	Test	Nº of signals	FO (min)	Duration (min)	Nº of intervals
34.5 kV	1	2626	150.5	155.1	32
	2	1015	180.9	186.1	38
	3	1646	111.0	112.6	23
	4*	**690**	**124.9**	**127.9**	**26**
	5	605	120.0	121.8	25
	6	360	118.0	119.4	24
	7	825	52.5	55.1	12
	8	2089	110.0	115.1	24
	9	1189	42.1	47.1	10
25 kV	1	4265	164.1	168.1	34
	2	23680	286.0	288.4	58
15 kV	1	964	80.1	84.1	17
	2	4639	177.0	180.9	37

of the type of insulator, the behavior of some analyzed variables showed a similar trend as the contamination evolved. Based on these observations, it was possible to establish three parameters (prior to the FO), from which different alert states can be defined based on the behavior of the PD measured with the UHF antenna.

To evaluate the performance of the three proposed parameters in the established alert states, 13 measurement processes were analyzed, nine with 34.5 kV class insulators, two with 25 kV class insulators, and two with 15 kV class insulators. Table I summarizes for the 13 measurement processes the number of signals measured, the time of occurrence of FO, the duration of each test, and the number of intervals of each test. The latter refers to the number of divisions of the test into 5-minute groups (intervals) to monitor the trends of the variables over time while saving memory resources.

As the time vector and the 5-minute arrays are established with the increase in PD activity, the variables from which the characteristic parameters of interest are extracted are also established. These variables are described below.

1) Cumulative Energy Per Interval: During the different measurement processes conducted on each of the insulators, significant variations were observed in the energy of the captured UHF signals. These variations were most pronounced at the beginning and end of the measurements (prior to the FO). To quantify and analyze this behavior, the accumulated energy per interval (CEI_k) was calculated for the entire measurement process. This energy is derived from each of the PD pulses, which are grouped into 5-minute intervals. This approach provides a general perspective on the energy dynamics of the PD UHF activity and it helps to determine whether it remains stable or increases over time compared to previous states.

First, the energy of each signal is calculated by the following equation:

$$E_j = \sum_{i=1}^{N} |x_i|^2 \tag{1}$$

where $E_{j\in\{1,\ldots,J\}}$ refers to the energy of the jth signal, being J the total of signals measured, $x_{i\in\{1,\ldots,N\}}$ is each point of the signal, and N corresponds to the length of the signal, in this case 5000. With the energy of all signals known, the total 5-minute array energy is obtained with the sum of all the E_j, as defined in the following equation:

$$E_k = \sum_{j=1}^{J} E_j. \tag{2}$$

The subindex $k \in \{1, 2, 3, \ldots, K\}$ indicates the kth 5-minute interval, being K the total amount of 5-minute intervals for that test. Finally, CEI_k in Fig. 4(a) is represented for each interval as the accumulate value of E_k, as shown in the following equation:

$$\mathrm{CEI}_k = \sum_{m=1}^{k} E_m. \tag{3}$$

In this way, every dot correlates to the accumulated energy value at the kth interval, which in this case (test 4*) reaches the 26th interval, as specified in Table I. The accumulated value shows how the trend develops over the elapsed time and counteracts particular instances where some signals within some intervals may proceed from external noise.

2) Cumulative Average Time Between Signals: As previously mentioned, during the UHF PD measurements, there were moments when the oscilloscope did not record any signal, defined as D_j. For each of the measurement processes, an increase in the occurrence of PD signals was observed once the contamination process with the sprayers was carried out (which reduces the dead time between discharges). The same behavior was evidenced as the contamination process progressed, as observed in Fig. 3, where the points become closer as the test advances.

Following the same subindex notation established for the previous variable, this time interval is measured between the signal x_j and x_{j+1}. The average time between signals of every D_j contained in the 5-minute kth interval (ATBS_k), calculated with (4), summarizes the amount of time that the acquisition system was waiting for the next signal

$$\mathrm{ATBS}_k = \frac{1}{J} \cdot \left(\sum_{j=1}^{J} D_j \right). \tag{4}$$

Although the repetition rate pattern is clear in Fig. 3, there had been some test runs where no EM pulses were perceived by the antenna near the end of the test, creating peaks of ATBS. This is tackled using the cumulative average time between signals, defined in (5), represented over the elapsed time (CATBS_k), as shown in Fig. 4(b).

$$\mathrm{CATBS}_k = \sum_{m=1}^{k} \mathrm{ATBS}_m. \tag{5}$$

Through this, variable is quantified the trend of the repetition rate of the PD EM activity measured by the antenna.

3) Cumulative Distributed Energy: This variable, CDE, is defined as the accumulated value of the distributed energy for each kth interval (DE_k), as shown in (6). DE_k is derived from the ratio between CEI_k and ATBS_k, which is a noncumulative value. Therefore, for this variable, we do not use cumulative values (CATBS) but rather the average value specifically obtained for each kth interval

$$\mathrm{DE}_k = \frac{\mathrm{CEI}_k}{\mathrm{ATBS}_k}. \tag{6}$$

The primary purpose of DE is to highlight the most notable trend changes in CEI and CATBS when combined. Thus, DE helps to identify more marked trend changes, compensating for any lack of trend observed in the CEI and ATBS values. This aspect is particularly useful for monitoring low-amplitude EM signals that barely exceed the trigger level. The trend of CDE is illustrated in Fig. 4(c), which shows the accumulated value of DE_k over time for the measurement process 4 taken as an example so far.

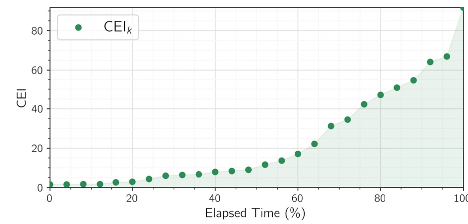

(a)

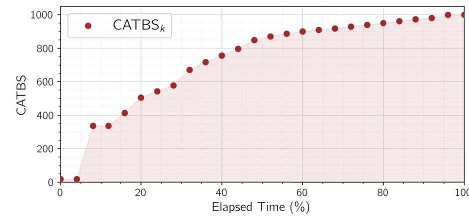

(b)

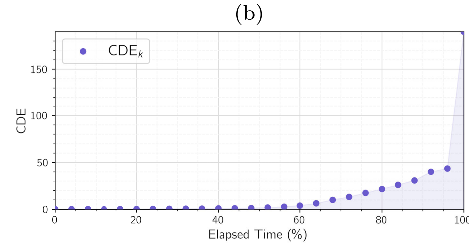

(c)

Fig. 4. (a) Cumulative energy per interval. (b) Cumulative average time between signals. (c) Cumulative distributed energy (max value of 189.9 at 100%) of the example test 4*.

C. Trend Change Indicators Recognition

To automatically identify and quantify trend changes in the previously described variables, and thereby establish the three indicators of interest, a segmented regression algorithm was applied to each variable. This innovative algorithm proposed by Muggeo [24], allows for the identification of changes or breakpoints in regression models that use a linear predictor [25]. Through the estimation of breakpoints, the algorithm fits linear regression models to data segments defined by these breakpoints. Muggeo [24] segmented regression was selected because the three derived series (CEI_k, CATBS_k, and CDE_k) are nonstationary and exhibit monotonic trends that are well approximated by continuous piecewise linear segments. Under these conditions, estimating explicit breakpoints and segment slopes yields interpretable ψ (expressed as % elapsed time) at low computational cost. The fit is applied to the first 95% of the elapsed time, excluding the final 5% associated with FO. In the experimental data, piecewise linear segmented fits achieved $R^2 > 0.95$ in most cases (as shown Section III-A).

The general definition is presented in (7), where x and y are the input vectors, α and c represent the slope and intercept of the first segment, respectively, β represents the change in slope from the first to the second segment, H is the

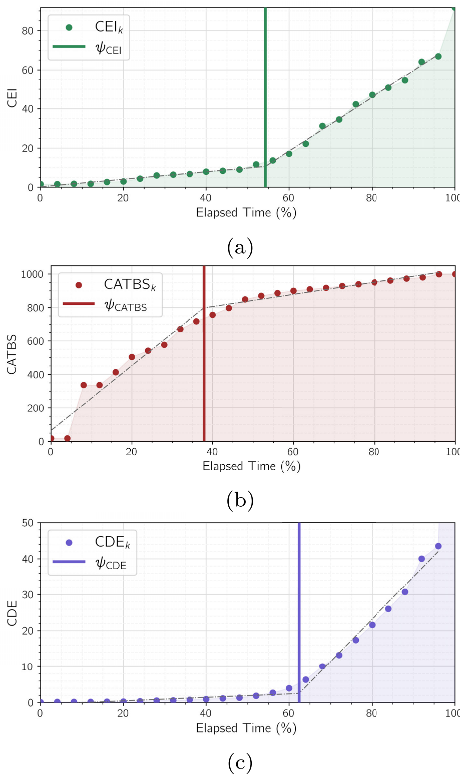

Fig. 5. Trend breakpoints of the example test 4* where (a) cumulative energy per interval, (b) cumulative average time between signals, and (c) cumulative distributed energy, with a max value of 189.9 at 100%.

Heaviside function that activates this change in the model at the breakpoint, ζ is a noise term, and ψ is the position of the breakpoint along the x vector

$$y = \alpha\, x + c + \beta\, (x - \psi)\; H\, (x - \psi) + \zeta. \tag{7}$$

The algorithm is capable of finding multiple segments through Taylor expansions. For example, segmented regression to identify a single breakpoint is carried out by means of a Taylor expansion in the vicinity of an estimated breakpoint, $\psi^{(0)}$, which transforms (7) into the following equation:

$$\begin{aligned} y \approx\;& \alpha\, x + c + \beta \left(x - \psi^{(0)}\right)\, H \left(x - \psi^{(0)}\right) \\ & - \beta \left(\psi - \psi^{(0)}\right)\, H \left(x - \psi^{(0)}\right) + \zeta. \end{aligned} \tag{8}$$

Considering the linear regressions fit to both segments, as well as the difference in their slopes and the noise term, the estimated breakpoint, $\psi^{(0)}$ is determined through an iterative process. Once the algorithm converges to a solution, a value of $|\beta| > 0$ indicates the existence of two distinct linear regressions on each side of the identified breakpoint. Additionally, a value of $\zeta \approx 0$ suggests that both segments meet at the same point, (x_ψ, y_ψ) at $\psi^{(0)}$. This way, trend changes (ψ) in CEI, CATBS, and CDE directly translate into the indicators that effectively signal the early occurrence of a FO event: ψ_{CEI}, ψ_{CATBS}, and ψ_{CDE}.

Finally, Fig. 5 shows the regression lines (gray dotted and dashed line) on both sides of the breakpoint (thick vertical line) found for measurement process 4, which has been used as an example so far. According to the figure, for the three variables CEI, CATBS, and CDE, the algorithm identifies a trend change near the middle of the measurement process (54.2% for ψ_{CEI}, 37.9% for ψ_{CATBS}, and 62.4% for ψ_{CDE}). It should be noted that during the FO, there is a sudden increase in the radiated and measured EM signals (as shown in Fig. 3); therefore, the algorithm is applied only to 95% of the elapsed time of each test, as the last 5% corresponds to the moment of FO. In practical terms, for an online monitoring system, the 5% would correspond to the most recently obtained data and the 95% to the historical record that has been collected through the variables.

Under wet-pollution conditions, a saline film builds up on the insulator surface and the surface conductivity increases with salinity and moisture. The resulting rise in leakage current and local field enhancement creates additional inception sites for PD along the contaminated path. As the process evolves, nonuniform heating promotes the formation of dry bands; larger voltage drops across these regions enable intermittent arc bridging. Within this framework, the detected breakpoints map to successive transitions: ψ_{CATBS} reflects the early increase in repetition rate (ATBS$_k$ decreases), ψ_{CEI} marks the growth in per-event energy consistent with dry-band arcing, and ψ_{CDE} emphasizes the combined rise of energy and repetition, typically appearing last and closer (among the three) to flashover (FO), without getting too close to the FO region, when arcing becomes quasi-continuous over the polluted surface. This reading is consistent with the UHF trends observed in the experiments (Section III).

D. Alert States Definition and Application Scenarios

It is worth emphasizing that the segmented regression model only requires two vectors and a specified number of estimated breakpoints as input data. Therefore, knowing the exact moment of the FO or the total elapsed time is not necessary to utilize the algorithm for trend change identification. This is particularly relevant in online measurement processes, where the FO moment is often unpredictable. Using the trend change information provided by segmented regression (ψ_{CEI}, ψ_{CATBS}, and ψ_{CDE}), we can establish rules with varying alert levels and activation criteria. These rules are applicable to insulators, considering the potential risk of FO. This depends on several factors, including equipment criticality, maintenance team response time (usually related to site accessibility), historical failure data, environmental conditions, equipment lifespan, and regulatory compliance standards.

From these factors, a robust, adaptive alert logic can be developed, aligned with the specific needs and risks associated with the monitored insulator's operation. Table II presents some possible real-world scenarios, considering the aforementioned considerations.

Scenario 1 could be applied, for instance, to insulators situated in remote or hard-to-reach areas, where any maintenance activity demands extensive logistical planning and extra resources. Consequently, it is recommended to establish an alert system based on these activation rules, wherein the initial alert is triggered upon detecting the first ψ.

TABLE II

Different Scenarios Arrangements to Define the Alert States According to the Number of Total Breakpoints (ψ) Found

Nº of ψ	**Scen. 1**	**Scen. 2**	**Scen. 3**	**Scen. 4**
0	Normal ●	Normal ●	Normal ●	Normal ●
1	Warning ●	Normal ●	Alarm ●	Attention ●
2	Warning ●	Warning ●	Alarm ●	Warning ●
3	Alarm ●	Alarm ●	Alarm ●	Alarm ●

Meanwhile, maintaining a *Warning* status with two ψ enables the maintenance team to monitor the situation and arrange an intervention before it escalates to a critical state. This precautionary measure helps avert an *Alarm* condition necessitating immediate and potentially urgent actions, which could incur greater disruption and cost.

Scenario 2 could be applied to easily accessible areas where a delayed maintenance alert may suffice, given that interventions can be swiftly carried out without extensive preparations. In such scenarios, quick response protocols can be established, ensuring that maintenance teams are equipped and prepared to act immediately upon receiving the alert, thus ensuring efficient management and minimizing downtime.

Scenario 3 may be associated with scenarios where the insulator operates in a highly critical system, such as those found in hospitals, data centers, or key infrastructures. Therefore, it is highly desirable to act promptly upon the first alert signal to perform rapid cleanings or repairs without disrupting service, thereby ensuring operational continuity.

At last, Scenario 4 can be applied to a large fleet of insulators characterized by diverse access levels for maintenance and criticality. This allows for the customization of multiple alert states to inform operational decisions. Depending on the identified state, operators can select from various response options, including scheduling detailed offline maintenance or implementing a rapid cleaning procedure. This modular approach facilitates operational flexibility and resource optimization by tailoring maintenance actions to the specific conditions of each insulator and its criticality within the electrical grid.

It is important to emphasize that the four scenarios described and the corresponding alert states proposed (*Normal*, *Attention*, *Warning*, and *Alarm*) are purely illustrative and should not be viewed as definitive or prescriptive models. These examples are intended to demonstrate how alert logics based on identified breakpoints could be configured. Therefore, the primary contribution of these scenarios is to showcase the potential of ψ as valuable indicators for monitoring and managing the need of maintenance of insulators in varying contexts. In practical terms, utilities have the flexibility to adapt or completely reformulate these cases and alert states to better suit their specific operational needs, local conditions, and internal policies. Thus, readers are encouraged to view ψ as an adaptable and scalable tool that can be seamlessly integrated into various risk management and maintenance frameworks. This facilitates more informed and contextualized decision-making processes related to fault prevention and operational response optimization.

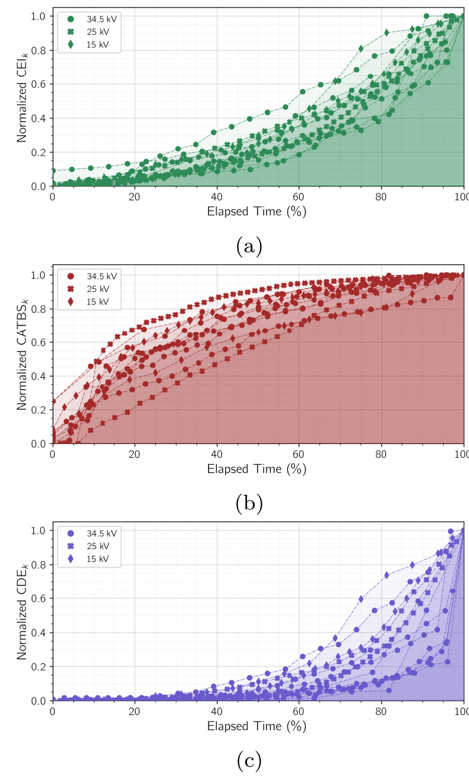

Fig. 6. Parameter summary for all 13 tests where (a) cumulative energy per interval, (b) cumulative average time between signals, and (c) cumulative distributed energy.

III. Results

For the experimental results presented below, Scenario 1 has been selected as the operating scenario for analyzing the 13 measurement processes conducted on three different types of insulators. In this scenario, the *Normal* alert state is the default state, where no ψ has yet been detected. At the first ψ, the alert state changes to *Warning*, at which time it is recommended to take measures to carry out the necessary maintenance maneuvers on the insulator. This state is maintained even when a second ψ occurs, understanding that maintenance procedures have already been initiated. Finally, when a third ψ is found, an *Alarm* state is issued, indicating an imminent FO event.

For comparative purposes only, the behavior of the three variables: CEI, CATBS, and CDE, was normalized based on the maximum magnitude obtained in each case. Fig. 6 summarizes the behavior of these variables for the three classes of insulators: 34.5, 25, and 15 kV (marked with a circle, a cross, and a diamond, respectively). Observing the three graphs in Fig. 6, it is clear that the variables exhibit a characteristic trend, regardless of the insulator class. For CEI and CDE, there appears to be an exponential trend, while for CATBS, a logarithmic behavior is observed. Furthermore, Fig. 6(a) show a generally uniform and smooth trend over time, while CDE in Fig. 6(b) displays a scattered behavior after the first half of the tests. These trend patterns indicate that UHF PD activity gradually increased in magnitude and repetition rate over time, reaching a critical point of change, implying that PD activity intensifies in the stages leading up to the FO event.

TABLE III

PERCENTAGE OF THE WHOLE ELAPSED TEST TIME IN WHICH THE DIFFERENT VARIABLES SHOWED A BREAKPOINT ψ (* TEST USED AS EXAMPLE)

Insulator Class	**Test Nº**	**Breakpoints** (%)			**Max breakpoint difference (%)**
		ψ_{CEI}	ψ_{CATBS}	ψ_{CDE}	
34.5 kV	1	51.1	55.0	59.5	8.5
	2	(24.7 ~ 68.2) 46.5	(12.4 ~ 65.9) 39.1	71.5	32.3
	3	43.7	39.1	56.3	17.2
	4*	**54.2**	**37.9**	**62.4**	**24.5**
	5	(46.4 ~ 78.1) 62.3	(18.5 ~ 51.7) 35.1	80.4	45.3
	6	(26.7 ~ 80.8) 53.8	25.3	(49.6 ~ 88.7) 69.2	43.9
	7	67.3	39.3	81.3	41.9
	8	15.6	16.0	58.6	43.0
	9	61.4	26.0	75.4	49.4
25 kV	1	71.0	70.8	(40.9 ~ 76.8) 58.8	12.2
	2	60.2	(15.3 ~ 46.5) 30.9	71.3	40.4
15 kV	1	42.8	33.4	53.3	19.8
	2	43.6	29.6	(45.7 ~ 76.3) 61.0	31.4
Average $\pm\sigma$		**51.8** $\pm$ 14.3	**36.7** $\pm$ 13.8	**66.1** $\pm$ 9.3	**31.5** $\pm$ 13.8

A. Trend Changes

When analyzing in Table III, the percentage of elapsed time during which a trend change occurred in the variables for the three types of insulators, it is observed that the ψ_{CATBS} indicator tends to appear in most of the measurement processes during the early stages of contamination, approximately at 37% of the average elapsed time since the start of the contamination process. On the other hand, ψ_{CEI} tends to occur around 52% of the elapsed time, and ψ_{CDE} manifests closer to the end of the test, around 66% of the elapsed time, without getting too close to the area where the FO event occurs. This latter point is clearly seen in Fig. 6(c), where for most of the measurement processes, minutes before the FO occurs, there is an increase in the energy of the signals and a decrease in the dead time between them, causing a sharp increase in the CDE values during the last 30% of the elapsed time.

The recommended criterion to determine if a parameter trend had one or more breakpoints (ψ) was the R-squared value of the segmented regression, selecting the one closest to 1. Generally, all the R-squared values from the obtained segmented regressions were above 0.95, with only one breakpoint in most cases. Nevertheless, in measurement processes 2, 5, and 6 conducted for the 34.5 kV class insulator, as well as in the two measurement processes for the 25 kV class insulator and the second measurement process for the 15 kV class insulator detailed in Table III, it was possible to find more than one breakpoint for the same variable. In these particular cases, both breakpoints were presented between parenthesis followed by the average value between them, established as the representative breakpoint of the whole trend.

The "Max Breakpoint Difference (%)" column in Table III reports, for each test, the interval between the earliest and the latest breakpoint among ψ_{CATBS}, ψ_{CEI}, and ψ_{CDE}. In all tests, this intra-run separation did not exceed 50% points. The consistent early-mid-late ordering and this meaningful separation support using the three indicators to define staged alert states related to the evolution of contamination and PD activity on the insulator surface.

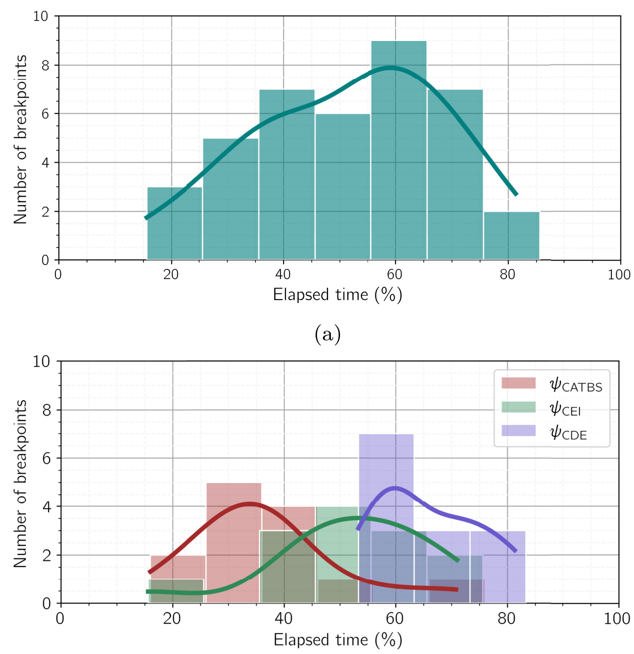

(a)

(b)

Fig. 7. Breakpoints histograms over time for all 13 tests. (a) All breakpoints together and (b) separated by indicators.

In Fig. 7, the data presented in Table III are graphically represented in histograms, where each bar covers 10% of the elapsed time. First, Fig. 7(a) displays all the breakpoints, without distinction, to illustrate the global trend pattern observed in all 13 tests. It is clear that all breakpoints were found after 15% of the elapsed time and before 85%, indicating that the three indicators anticipate the occurrence of each FO event. Generally, as evidenced in this figure, these trend changes or breakpoints were most commonly observed around 60% of the test duration. Second, by classifying each breakpoint according to its parameter, the histogram in Fig. 7(b) highlights the trend change pattern of each indicator and relates its distribution to

TABLE IV

ALERT STATES ACCORDING TO THE RISK OF FO (* TEST USED AS EXAMPLE)

Insulator Class	Test Nº	Change of State (%)	
		Warning	Alarm
34.5 kV	1	51.1	59.5
	2	39.1	71.5
	3	39.1	56.3
	4*	**37.9**	**62.4**
	5	35.1	80.4
	6	25.3	69.2
	7	39.3	81.3
	8	15.6	58.6
	9	26.0	75.4
Average 34.5 **kV** $\pm\ \sigma$		**34.3** $\pm$ 10.4	**68.3** $\pm$ 9.5
25 kV	1	58.8	71.0
	2	30.9	71.3
Average 25 **kV** $\pm\ \sigma$		**44.9** $\pm$ 19.7	**71.2** $\pm$ 0.2
15 kV	1	33.4	53.3
	2	29.6	61.0
Average 15 **kV** $\pm\ \sigma$		**31.5** $\pm$ 2.7	**57.2** $\pm$ 5.4
Overall average $\pm\ \sigma$		**35.5** $\pm$ 11.1	**67.0** $\pm$ 9.1

its average value previously presented in Table III. As shown in Fig. 7(b), the first indicator, ψ_{CATBS}, has the highest repetition rate and shows a first trend change (breakpoint) around 37% of the elapsed time. It is followed by ψ_{CEI}, which is the second indicator to show a trend change in PD activity on the insulator surface, being more likely near the midpoint of the elapsed time. At last, ψ_{CDE} is the final parameter to demonstrate a trend change, around 66% of the elapsed time, consistent with what is shown in Table III.

B. Alert States

The alert states for each test are detailed in Table IV, where the *Warning* and *Alarm* columns show the state of time at which each indicator was activated in each experiment, as contamination increased on the insulator and Scenario 1 was used as the operating state. Observing the histogram distribution in Fig. 7(b), a clear behavioral pattern was identified, where the first breakpoint generally corresponded to ψ_{CATBS}, and the last to ψ_{CDE}. Based on this behavior, the *Warning* state was established 77% of the time by ψ_{CATBS} (in ten out of the 13 experiments), followed by ψ_{CEI} with 15%. As for the critical *Alarm* state, 92% of the time, it was set by ψ_{CDE} and 8% by ψ_{CEI}. This indicates that most often, the *Warning* state is activated by an increase in the occurrence rate of PD, and the *Alarm* state is generally triggered by an increase in the PD energy. The average state change values in Table IV show that the parameters have similar behavior regardless of the insulator class, demonstrating that UHF PD activity on a contaminated insulator has a characteristic tendency that can be effectively quantified by these indicators.

On average, the *Warning* state occurs at 35.5% of the elapsed time, while the *Alarm* state at 67%. Both values have a standard deviation below 15%, which for the longest test (288 min) implies a time variation of 43 min, and for the shortest (47 min) 7 min. Particularly, the largest gap obtained between the *Warning* and *Alarm* states is 49.4% of the elapsed time, while the shortest is 12.2%. In any case, for quantifying stochastic behavior, this system offers a well-defined prediction regardless of the test duration. In all tests, all breakpoints were found before 80% of the elapsed test time, meaning that in all of them, the FO occurred in an *Alarm* state.

As mentioned in Section II-A, the experiments were conducted in such a way that the contamination process, which normally could take months, was accelerated to last just a couple of hours. Since the maximum breakpoint difference calculated in Table III is equal to the time difference (percentage of elapsed time) between the warning and alert states, the average time between changes from *Warning* to *Alarm* states is 31.5%. In a real application, this percentage of time provides the operator with an adequate time window to take the necessary maintenance measures to prevent a potential FO event on the insulator.

C. Scope, Flexibility, and Implementation Challenges

As evidenced in Section III-B, the proposed approach is not based on exhaustive waveform fitting but on tracking its temporal evolution through three indicators (CEI_k, CATBS_k, and CDE_k) and on detecting regime changes with segmented regression (ψ). These ψ are assigned to alert states by means of configurable rules that can be adjusted according to asset criticality, accessibility, and response times, failure history, and environmental or operational conditions, enabling maintenance strategies tailored to each installation. Likewise, the four alert states and the four proposed scenarios can be reduced or expanded according to maintenance program needs without modifying the measurement hardware.

In comparison with certain leakage-current-based methods (analytical or AI-driven) [20], [26], [27], [28], [29], and with approaches based on conventional PD measurement or optical/ultrasonic techniques that require local couplings or multiple sensors [22], [30], [31], the proposed system is non-invasive, has low computational burden, and does not require training phases, practical attributes for online operation.

That said, bringing the system into real operating conditions raises challenges that go beyond those anticipated at the laboratory level. It is necessary to consider design factors (insulator material and geometry), environmental aspects, instrumentation, and asset operation. Ceramic or glass insulators (more hydrophilic) favor the formation of conductive films under high humidity, with more distributed PD activity. In turn, polymeric insulators (more hydrophobic) tend to limit conductive points, although under severe conditions or prolonged exposure hydrophobicity may degrade and more localized and intense discharges may appear. The diversity of contaminants such as dust, soot, or salt in industrial or coastal environments alters surface resistivity and signal propagation, modifying the patterns captured. In addition, the type, orientation, and location of the antenna, together with electrical/electromagnetic noise in the environment (frequently high and variable), require prior and periodic characterization, as well as reference profiles that allow setting thresholds and persistence times specific to each site [31].

IV. Conclusion

This work presented a noninvasive early-warning methodology for FO in contaminated insulators, based on three indicators obtained from UHF PD measurements (CEI_k, $CATBS_k$, and CDE_k) and on detecting trend changes via segmented regression. The novelty lies in integrating cumulative indicators and, from their breakpoints (ψ), mapping adjustable alert states without requiring prior training or galvanic contact, with low computational requirements and applicable to online measurements over a historical window.

In 13 tests and three classes of insulators, the breakpoints showed a consistent temporal order over the course of the test ($\psi_{\mathrm{CATBS}} \approx 37\%$, $\psi_{\mathrm{CEI}} \approx 52\%$, and $\psi_{\mathrm{CDE}} \approx 66\%$). With the adopted operating logic, the system issued a *Warning* at average at 35.5% and *Alarm* at 67% of the test duration, while FO events clustered near 80%. In all tests, FO occurred when the system was already in the *Alarm* state. These figures delineate a useful intervention window, since there is a consistent interval between *Warning* and *Alarm*, followed by an additional margin between *Alarm* and FO, which offers a realistic opportunity for preventive actions.

Taken together, the indicator-breakpoint-state combination constitutes an interpretable and practically deployable tool to support the operation and maintenance of insulators, with thresholds and scenarios that can be adjusted to asset criticality, accessibility, response times, and environmental conditions without hardware changes. Future work should validate the methodology in other materials (ceramic, glass, and polymeric insulators) and under field conditions with varying contamination levels and operating environments. In addition, thresholds and persistence times should be adjusted on a per-site basis, considering the profile of electrical and electromagnetic noise and the available instrumentation (type and location of the antenna).

References

[1] Selection and Dimensioning of High-Voltage Insulators Intended for Use in Polluted Conditions, Standard IEC 60815, 2009.

[2] Polluted Insulators: A Review of Current Knowledge, Standard TF 33.04.01, CIGRE, 2000.

[3] J. M. Seifert et al., "Methods for dielectric characterization of polymeric insulating materials for outdoor applications," Conseil Int. des Grands Réseaux Électriques (CIGRE), Paris, France, Tech. Brochure (TB) 822, 2020.

[4] E. Kuffel and W. S. Zaengl, *High-Voltage Engineering*. Oxford, U.K.: Pergamon Press, 1984.

[5] F. Obenaus, "Fremdschichtüberschlag und Kriechweglänge," *Deutsche Elektrotechnik*, vol. 4, pp. 135–136, 1958.

[6] L. L. Alston and S. Zoledziowski, "Growth of discharges on polluted insulation," *Proc. Inst. Electr. Engineers*, vol. 110, no. 7, p. 1260, 1963.

[7] L. Orellana, J. Ardila-Rey, G. Avaria, and S. Davis, "Danger assessment of the partial discharges temporal evolution on a polluted insulator using UHF measurement and deep learning," *Eng. Appl. Artif. Intell.*, vol. 124, Sep. 2023, Art. no. 106573. [Online]. Available: https://linkinghub.elsevier.com/retrieve/pii/S0952197623007571

[8] S. Lu, H. Chai, A. Sahoo, and B. T. Phung, "Condition monitoring based on partial discharge diagnostics using machine learning methods: A comprehensive state-of-the-art review," *IEEE Trans. Dielectr. Electr. Insul.*, vol. 27, no. 6, pp. 1861–1888, Dec. 2020.

[9] Y. Li, B. Hu, S. Wei, D. Gao, and F. Shuang, "Simplify-YOLOv5m: A simplified high-speed insulator detection algorithm for UAV images," *IEEE Trans. Instrum. Meas.*, vol. 74, pp. 1–14, 2025.

[10] S. C. Oliveira and E. Fontana, "Optical detection of partial discharges on insulator strings of high-voltage transmission lines," *IEEE Trans. Instrum. Meas.*, vol. 58, no. 7, pp. 2328–2334, Jul. 2009.

[11] Artificial Pollution Tests on High-voltage Ceramic and Glass Insulators To Be Used on AC Systems, Standard IEC 60507, 2018.

[12] Pollution Test of Naturally and Artificially Contaminated Insulators, Standard WG D1.44, CIGRE, 2017.

[13] F. Álvarez, F. Garnacho, J. Ortego, and M. Sánchez-Urán, "Application of HFCT and UHF sensors in on-line partial discharge measurements for insulation diagnosis of high voltage equipment," *Sensors*, vol. 15, no. 4, pp. 7360–7387, Mar. 2015.

[14] S. Chandrasekar, C. Kalaivanan, G. Montanari, and A. Cavallini, "Partial discharge detection as a tool to infer pollution severity of polymeric insulators," *IEEE Trans. Dielectr. Electr. Insul.*, vol. 17, no. 1, pp. 181–188, Feb. 2010.

[15] J. Li, W. Sima, C. Sun, and S. A. Sebo, "Use of leakage currents of insulators to determine the stage characteristics of the flashover process and contamination level prediction," *IEEE Trans. Dielectr. Electr. Insul.*, vol. 17, no. 2, pp. 490–501, Apr. 2010.

[16] High Voltage Test Techniques. Measurement of Partial Discharges By Electromagnetic and Acoustic Methods, Standard IEC 62478, 2016.

[17] *Guidelines for Partial Discharge Detection Using Conventional (IEC 60270) Unconventional Methods*, CIGRE, 2016.

[18] R. Albarracín Sánchez, "Medida de descargas parciales en radiofrecuencia," Ph.D. dissertation, Universidad Carlos III de Madrid, Madrid, Spain, 2014. [Online]. Available: https://e-archivo.uc3m.es/handle/10016/18998

[19] S. Russell and P. Norvig, *Artificial Intelligence—A Modern Approach*. London, U.K.: Pearson, 2020.

[20] S. Zhao, X. Jiang, Z. Zhang, J. Hu, and L. Shu, "Flashover voltage prediction of composite insulators based on the characteristics of leakage current," *IEEE Trans. Power Del.*, vol. 28, no. 3, pp. 1699–1708, Jul. 2013. [Online]. Available: http://ieeexplore.ieee.org

[21] Narmadhai, "Analysis of leakage current to predict insulator flashover using artificial neural network," *J. Comput. Sci.*, vol. 7, no. 2, pp. 167–172, Feb. 2011.

[22] S. F. Stefenon, R. Bruns, A. Sartori, L. H. Meyer, R. G. Ovejero, and V. R. Q. Leithardt, "Analysis of the ultrasonic signal in polymeric contaminated insulators through ensemble learning methods," *IEEE Access*, vol. 10, pp. 33980–33991, 2022.

[23] *High-voltage Test Techniques-Partial Discharge Measurements*, 2001.

[24] V. M. R. Muggeo, "Estimating regression models with unknown break-points," *Statist. Med.*, vol. 22, no. 19, pp. 3055–3071, Oct. 2003.

[25] C. Pilgrim, "Piecewise-regression (aka segmented regression) in Python," *J. Open Source Softw.*, vol. 6, no. 68, p. 3859, Dec. 2021.

[26] Z. Yang, X. Jiang, Z. Zhang, D. Zhang, and Y. Liu, "Study on the influence rules of soluble contaminants on flashover voltage of disc suspension insulators," *IEEE Trans. Dielectr. Electr. Insul.*, vol. 23, no. 6, pp. 3523–3530, Dec. 2016.

[27] L. Cui, R. S. Gorur, and D. Chipman, "Evaluating flashover performance of insulators under fire fighting conditions," *IEEE Trans. Dielectr. Electr. Insul.*, vol. 24, no. 2, pp. 1051–1056, Apr. 2017.

[28] N. F. Sopelsa Neto, S. F. Stefenon, L. H. Meyer, R. G. Ovejero, and V. R. Q. Leithardt, "Fault prediction based on leakage current in contaminated insulators using enhanced time series forecasting models," *Sensors*, vol. 22, no. 16, p. 6121, Aug. 2022. [Online]. Available: https://www.mdpi.com/1424-8220/22/16/6121

[29] H. R. Sezavar, N. Fahimi, S. Hasanzadeh, and A. A. S. Akmal, "Risk assessment of contaminated composite insulators in pre-flashover conditions," *Electric Power Syst. Res.*, vol. 230, May 2024, Art. no. 110256. [Online]. Available: https://www.sciencedirect.com/science/article/pii/S0378779624001445

[30] J. M. de Barros Bezerra, A. M. N. Lima, G. S. Deep, and E. G. da Costa, "An evaluation of alternative techniques for monitoring insulator pollution," *IEEE Trans. Power Del.*, vol. 24, no. 4, pp. 1773–1780, Oct. 2009.

[31] J. A. Ardila-Rey, C. A. Jorquera, J. P. Gómez, B. A. de Castro, S. Govindarajan, and L. Orellana, "A hybrid CNN-LSTM model for flashover alert on polluted insulators using UHF and acoustic PD signals," *IEEE Trans. Instrum. Meas.*, vol. 74, pp. 1–16, 2025.